Capillarity

Vol. 19, No. 1, p. 1-14, 2026

Original article

Nitrogen- and chemical-assisted steam huff-and-puff of heavy oil in heterogeneous microfluidic pore network

Tao Wei[1], Jianmei Yu[1], Qiuying Cao[1], Wenjie Han[1], Jinping Liang[1], Rui Wu[2]*

[1]*Exploration and Development Research Institute, Dongying 257100, P. R. China*

[2]*School of Mechanical Engineering, Shanghai Jiao Tong University, Shanghai 200240, P. R. China*

Keywords:
Heavy oil
steam huff-and-puff
thermal recovery
microfluidic pore network

Cited as:
Wei, T., Yu, J., Cao, Q., Han, W., Liang, J., Wu, R. Nitrogen- and chemical-assisted steam huff-and-puff of heavy oil in heterogeneous microfluidic pore network. Capillarity, 2026, 19(1): 1-14.
https://doi.org/10.46690/capi.2026.04.01

Abstract:
Steam huff-and-puff has been widely applied for heavy-oil thermal recovery. However, the opacity of reservoir rocks limits direct pore-scale observation of oil mobilization, hindering the evaluation and optimization of co-injected fluids. To address this issue, a microfluidic experimental system is developed to simulate authentic reservoir huff-and-puff conditions, enabling the pore-scale investigation of steam-based oil recovery assisted by nitrogen and an oil displacement agent. The pore network used in our experiments features both low-permeability and high-permeability zones. In single-fluid injection experiments, stable flow channels form predominantly in the high-permeability zone, thereby limiting overall heavy oil mobilization. When multiple fluids are injected, however, the injection sequence proves to be highly influential. In a dual-fluid injection of oil displacement agent followed by nitrogen, emulsion and oil-in-microbubble cluster are formed, significantly improving oil mobility. In a ternary injection of nitrogen followed by oil displacement agent and steam, although steam reduces oil viscosity by raising the temperature, the accompanying condensate dilutes the oil displacement agent and thus affects its interactions with heavy oil and gas. These results clarify the role of injection fluids and their sequence in the nitrogen- and chemical-assisted steam huff-and-puff of heavy oil, providing important insights for the optimization of heavy oil recovery strategies.

1. Introduction

Heavy oil accounts for approximately 50% of all hydrocarbon reserves (Li et al., 2020; Gomaa et al., 2024; Xiong et al., 2024). However, its extraction is more challenging than that of conventional light oil due to its high viscosity. Since viscosity decreases with rising temperature, thermal recovery techniques have been commonly employed for heavy oil extraction (Pratama and Babadagli, 2022; Ahmadi and Chen, 2020; Gomaa et al., 2024). Among them, steam huff-and-puff is an important method, which makes up 80% of the thermal recovery of heavy oil in China (Hu et al., 2005; He et al., 2022; Zhang et al., 2026). Therein, steam is injected into the reservoir from a well, soaked for a while, and then opened again for oil extraction (Fan et al., 2021; Tao et al., 2022; Zou et al., 2022). To enhance recovery, gases (such as N_2) and chemicals have also been co-injected with steam (Wan et al., 2020; Xiong et al., 2022; Bai et al., 2025). Such N_2- and chemical-assisted steam huff-and-puff techniques have been successfully employed by the Shengli Oilfield Company to extract heavy oil (Gao et al., 2014; Wei et al., 2020; Hao et al., 2021). In their field applications targeting a thin-layered ultra-heavy oil reservoir in Xinjiang, N_2 is used as the gas and an oil-displacement agent (ODA) as the chemical additive.

Yandy Scientific Press

*Corresponding author.
E-mail address: weitao819.slyt@sinopec.com (T. Wei); yujianmei228.slyt@sinopec.com (J. Yu); caoqiuying.slyt@sinopec.com (Q. Cao); hanwenjie.slyt@sinopec.com (W. Han); liangjinping.slyt@sinopec.com (J. Liang); ruiwu@sjtu.edu.cn (R. Wu).

Received January 13, 2026; revised February 8, 2026; accepted March 1, 2026; available online March 5, 2026.

Nonetheless, to optimize the injection protocol for gas- and chemical-assisted steam huff-and-puff, it is essential to have a detailed understanding of how these agents influence heavy oil movement within reservoir pores.

Visualization experiments are crucial for observing heavy oil behavior at the pore scale. Two main types of such experiments have so far been reported in the literature: Micro-computed tomography (micro-CT) (Mahardika et al., 2021; Su et al., 2022) and microfluidics-based pore network studies (Vavra et al., 2020; Wang et al., 2022). While micro-CT allows the use of real porous materials, microfluidic experiments typically employ quasi-two-dimensional pore networks and thus offer higher spatial and temporal resolution. Therefore, microfluidic methods are better suited for capturing the detailed dynamics of heavy oil movement in reservoir pores. Several microfluidic studies have investigated the effects of surfactants, alkali–cosolvent mixtures, alkali–cosolvent–polymer systems, and calcium hydroxide on heavy oil displacement during flooding (Schumi et al., 2020; Arabloo et al., 2024; Li et al., 2024).

Despite the extensive use of microfluidics in light oil recovery research (Lu et al., 2021; Guo et al., 2022; Huang et al., 2020), its application to huff-and-puff processes in heavy oil systems remains underexplored. Previous studies have suggested that in shale fracture networks, gas expansion is a primary driver of light oil mobilization during N_2 huff-and-puff (Nguyen et al., 2018; Gong et al., 2020; He et al., 2021). In thin-layered heavy oil reservoirs, the co-injection of N_2 or chemicals with steam has been observed to form a gas cap above the oil layer, reducing heat loss (Owolabi and Dyam, 2012; Wang et al., 2023; Sun et al., 2024). Building on the findings of Nguyen et al. (2018), in this study, it is hypothesized that gas expansion may also play a role in enhancing heavy oil recovery during huff-and-puff operations. This raises several questions: Does gas expansion occur during steam huff-and-puff? If so, does it meaningfully contribute to oil recovery? How do steam and ODA influence this process? Addressing these questions requires pore-scale investigations using microfluidic experiments that simulate N_2 and chemical-assisted steam huff-and-puff in heavy oil systems.

To ensure representativeness, such microfluidic experiments must be conducted under temperature and pressure conditions closely resembling those found in actual reservoirs (Bao et al., 2017; Saadat et al., 2021; Lei et al., 2022). For example, Xu et al. (2018) developed a microfluidic system operating at approximately 180 °C and 1 MPa to study steam-assisted gravity drainage in bitumen. In field applications of N_2- and chemical-assisted steam huff-and-puff in thin-layer heavy oil reservoirs, steam at around 300 °C is typically injected into reservoirs with pressures near 2 MPa. Although high-pressure microfluidic experiments up to 50 MPa are feasible when using overburden pressure cells (Gizzatov et al., 2021; Yu et al., 2022; Li et al., 2024), such setups hinder direct temperature measurement at the pore network surface via thermal cameras. Given that temperature critically affects heavy oil viscosity and steam condensation, obtaining pore-scale temperature distributions is essential. This calls for the development of a new microfluidic pore network model that is capable of withstanding internal–external pressure differences exceeding 2 MPa without external confinement, thereby enabling accurate thermal monitoring.

To address the above need, this study introduces a novel high-pressure, high-temperature microfluidic platform designed to reveal pore-scale dynamics during N_2- and chemical-assisted steam huff-and-puff in heavy oil systems. This platform successfully replicates harsh reservoir conditions, including steam temperatures of 300 °C and pressures above 2 MPa. The resulting insights provide a mechanistic understanding to support the design of more efficient heavy oil recovery strategies. The paper is structured as follows: Section 2 describes the experimental methods and procedures, Section 3 presents the key findings, and Section 4 summarizes the conclusions and their practical implications.

2. Experiments

To ensure that the microfluidic experiments yield meaningful insights, they must be designed as representative analogs of the reservoir. This necessitates that the pore structure, fluid properties, operating conditions, and key dimensionless parameters need to closely match those of the target field application. The following subsections outline our experimental design, setup and procedures in detail.

2.1 Design of microfluidic experiments

2.1.1 Pore network structures

The fluids used in the microfluidic experiments were identical to those employed in the corresponding field applications. Both the heavy oil and the ODA (oil displacement agent) were provided by the Shengli Oilfield Company. The viscosity of the heavy oil used, measured using a digital rotational rheometer (Brookfield DV2T), exhibits strong temperature dependence: 10 Pa·s at 30 °C, 1 Pa·s at 50 °C, 0.5 Pa·s at 70 °C, and 0.2 Pa·s at 90 °C (Fig. S1). The ODA is a hydrophilic surfactant solution, whose physical properties, such as viscosity and density, are similar to those of water at the ambient conditions. The interface tension (IFT) between the heavy oil and ODA was measured using a spinning drop tensiometer (TX500C+). The ODA can reduce the IFT to ultralow levels, which were 1.6×10^{-3} mN/m at 60 °C, 1.1×10^{-3} mN/m at 90 °C, and 9.5×10^{-4} mN/m at 120 °C (Fig. S2). Moreover, the ODA reduces the viscosity of heavy oil by 93.78%. It should be noted that this ODA has not yet commercialized; thus, detailed information regarding its chemical composition could not be disclosed in this paper.

To accurately replicate the reservoir conditions, the pore network used in the microfluidic experiments was carefully designed to reflect both the pore structure and wettability of the target oil reservoir. For pore structure characterization, particle size analysis was conducted on reservoir rock samples using a laser particle size analyzer (Malvern Mastersizer 3000). The results indicated pronounced heterogeneity, with particle sizes ranging from 52 to 350 μm (Fig. S3). In addition, the wettability of the rock particles was evaluated using a contact angle goniometer (KRUSS DSA25S), which confirmed the predominantly oleophilic nature of the formation (Fig. S4).

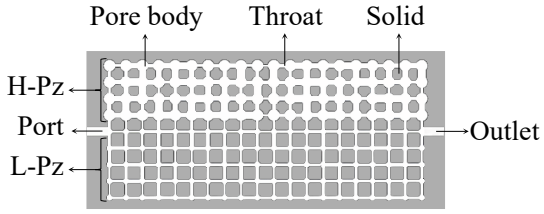

Fig. 1. Schematic of the quasi-two-dimensional microfluidic pore network used in this study. Here, H-Pz means high-permeability zone, and L-Pz denotes low-permeability zone.

The pore network utilized in this study consisted of pore bodies and pore throats, as shown in Fig. 1. All pores feature a uniform thickness of 50 μm in the direction perpendicular to the plane of this figure. Accordingly, the following description of the pore network structure emphasizes the two-dimensional geometry depicted in Fig. 1. The pore bodies are circular and are interconnected by rectangular pore throats. The distance between the centers of two adjacent pore bodies is 1 mm. To reflect the natural heterogeneity of the reservoir rock, the pore network was divided into two distinct zones: A low-permeability region and a high-permeability region. In the low-permeability region, all pore bodies have a diameter of 700 μm, and the pore throat widths are uniformly distributed between 320 and 500 μm. In the high-permeability region, all pore bodies have a diameter of 350 μm, with pore throat widths uniformly ranging from 160 to 250 μm. On one side of the network, a pore body is connected to an inlet port through for fluid injection. On the opposite side, another pore body is connected to an outlet channel, which is linked to a valve as illustrated in Fig. 2.

The designed pore network was fabricated using chromium mask etching on a 490 mm × 200 mm BF33 borosilicate glass substrate (Zhenjiang Huarui Chip Technology Co., Ltd.). Quartz glass (BF33) was selected due to its oleophilic affinity toward heavy oil (Fig. S5). The detailed fabrication procedures can be found in the work of De Haas et al. (2013).

2.1.2 Injection fluids and velocity

The viscosity ratio (M) and capillary number (Ca) are two key parameters governing multiphase flow in porous media. To ensure representative flow conditions, the values of these two parameters in our microfluidic experiments should correspond to those in practical applications. The viscosity ratio is defined as the ratio of the viscosity of the injected fluid to that of the heavy oil (Heijkoop et al., 2024).

$$M = \frac{\mu_f}{\mu_o} \tag{1}$$

where μ_f denotes the viscosity of the injection fluid and μ_o denotes the viscosity of heavy oil. Since the same fluids were used in both the microfluidic experiments and the practical applications, their viscosity ratios were the same.

The capillary number is defined as the ratio of viscous forces to capillary forces (McBride et al., 2025).

$$\mathrm{Ca} = \frac{\mu_f u}{\gamma} \tag{2}$$

where u represents the fluid velocity and γ is the interfacial tension between the injected fluid and the heavy oil. To eliminate the influence of temperature-dependent heavy oil viscosity, the displacing fluid viscosity was used to evaluate the capillary number. To ensure that the capillary number remained the same in both the microfluidic experiments and the practical reservoir conditions, the same fluid velocity was used:

$$u_c = u_r \tag{3}$$

where the subscript c and r denote the microfluidic pore network and reservoir, respectively. The fluid velocity, u, is defined as:

$$u = \frac{q}{A} \tag{4}$$

where q represents the flow rate of injected fluid and A denotes the cross-sectional area of the zone swept by the injected fluid. In the field applications considered here, A_r was taken as 500 m^2 for the unit zone based on the well configuration provided by the Shengli Oilfield Company, as illustrated in Fig. S6 (the size of the unit zone is 200 m × 100 m × 5 m). The corresponding flow rates q_r for the unit zone are 8×10^3 kg/h for steam, 1.75×10^5 kg/h for N_2, and 20 kg/h for ODA. The cross-sectional area of the pore network used in our microfluidic experiments is $A_c = 8.525$ mm × 50 μm (the size is 19.7 mm × 8.525 mm × 50 μm). Therefore, using the equivalence $u_c = u_r$ as well as Eq. (4), the corresponding flow rates in the microfluidic experiments are 6.78×10^{-6} kg/h (i.e., 3.76×10^{-3} mL/min) for steam, 1.50×10^{-4} kg/h for N_2 (i.e., 3.33×10^{-2} mL/min), and 1.7×10^{-8} kg/h (i.e., 2.97×10^{-7} mL/min) for ODA.

The relationship between the mass of fluid injected in microfluidic experiments and that in field applications can be expressed as (Rayleigh, 1915):

$$\frac{m_c}{m_r} = \frac{V_c}{V_r} \tag{5}$$

where m represents the mass of injected fluid and V is the volume of the zone swept by the injected fluid. In field applications, m_r is 2.2×10^6 kg for steam, 5.83×10^7 kg for N_2 (at standard condition), and 2×10^4 kg for ODA. Taking the size of swept zones mentioned above as a basis, V_c/V_r is 8.4×10^{-14}. Therefore, the corresponding mass of fluid required in the microfluidic experiments, m_c, was 1.85×10^{-7} kg for steam, 4.90×10^{-6} kg for N_2, and 1.68×10^{-9} kg for ODA. A comparison of the injection parameters between the microfluidic experiments and field applications is summarized in Table 1.

2.2 Experimental setup

The microfluidic experimental setup comprised three main modules, as illustrated in Fig. 2: A heavy oil injection module, a working fluid injection module, and a visualization module. These modules were interconnected via a series of valves and stainless-steel tubing (1 mm inner diameter, 1/16 inch outer diameter).

In the heavy oil injection module, a syringe pump (Pump 11 Elite, Harvard Apparatus, USA) was employed to deliver

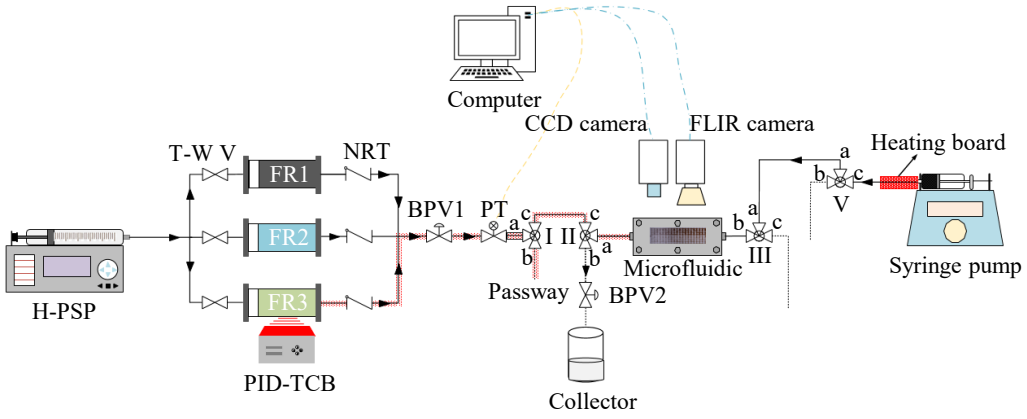

Fig. 2. Schematic of the microfluidic visualization experimental system. The yellow dashed lines represent the signal transmission lines for the pressure transducer, while the blue dashed lines denote the data connection cables for the high-definition (HD) and infrared (IR) cameras. T-WV: Two-way valve; FR1-3: Fluid reservoirs, consisting of oil displacement agent (FR1), nitrogen (FR2), and deionized water (FR3), respectively; NRT: Non-return valve; BPV1-2: Back pressure valves; PT: Pressure transducer; I-V: Three-way directional valves. H-PSP refers to the high-pressure syringe pump; PID-TCB denotes the PID temperature control box.

Table 1. Comparison of injection parameters for microfluidic experiments and field applications.

Fluid	m_r (kg)	q_r (kg/h)	m_c (kg)	q_c (kg/h)	u (m/s)
Steam	2.2×10^6	8×10^3	1.85×10^{-7}	6.78×10^{-6}	1.48×10^{-4}
N_2	5.83×10^7	1.75×10^5	4.90×10^{-6}	1.50×10^{-4}	1.35×10^{-3}
ODA	2×10^4	20	1.68×10^{-9}	1.7×10^{-8}	1.11×10^{-8}

heavy oil into the microfluidic pore network. During injection, the syringe was heated to 45 °C via silicone heating tapes to reduce the oil viscosity, so as to ensure stable flow. A three-way valve (SS-731FK1, XiongChuan, China) was installed between the syringe pump and the pore network to control flow direction.

The working fluid injection module consisted of a high-pressure syringe pump (Fusion 6000, Chemyx, USA), fluid reservoirs, and a set of flow control valves (check, two-way, and three-way valves; Xiong Chuan-SS, China). A PID temperature controller (X200, XingHaomai, China) was employed to generate steam. The pressure of the injection fluid was measured by a pressure transducer (PMP5023-TB-A3-CB-H0-PA, ±10 MPa, Omega, USA), and the flow rate was controlled by a high-pressure syringe pump.

The visualization module integrates optical and thermal imaging to monitor the experimental process. A Nikon D810 camera equipped with a macro lens (AF-S VR Micro-Nikkor 105 mm f/2.8G IF-ED, Japan) was used to record the fluid distribution within the pore network, while an infrared camera (FLIR A600, USA) was used to capture the corresponding temperature distribution at its surface. Illumination was provided by a cold light source. The microfluidic pore network itself was mounted inside a custom aluminum fixture, which enabled the pore network to withstand internal pressures of up to 10 MPa. An exploded view detailing the assembly of the fixture and pore network is presented in Fig. S7.

2.3 Experimental procedure

The experimental procedure was performed according to the following steps:

(1) Air purging

Prior to experimentation, three-way valves I and II were configured to open ports a and c, while valve III and V were configured to open ports a and b. Deionized water (or N_2 in the N_2-only injection experiment) was then injected into the system using a high-pressure syringe pump, flushing the flow line from the pump to three-way valve V so as to remove air from the system.

(2) Heavy oil injection

First, ports a and c on valves III and V were opened, and heavy oil was injected at a constant rate of 10 μL/min to completely remove any water and residual gas from the pipeline between these valves. Then, ports a and c on valve V, ports a and b on valve III, and ports a and b on valve II were opened. The back pressure valve (BPV-2) was set to 2 MPa. Heavy oil was then injected into the pore network at a constant rate of 10 μL/min until it reached the collector, ensuring that the pore network was fully saturated and stabilized at an initial reservoir pressure of 2 MPa.

(3) Working fluids injection

Before injecting working fluids for the huff-and-puff process, valves I were configured to open ports a and c, and valves II were configured to open ports c and b. Any water remaining in the pipe between the high-pressure syringe pump and valve

Table 2. Experimental conditions and oil extraction after the first cycle of huff-n-puff.

Injected fluid	T_c (°C)	P_f (MPa)	Apparent recovery rate (%)
[A] Water	50	6.05	0
[B] Water	70	6.11	16.22
[C] Steam	26	6.08	0
[D] N_2	26	1.84	0
[E] ODA	26	6.13	0
[F] ODA-N_2	26	6.13/1.84	30.05
[G] ODA-Steam	26	6.13/6.08	0
[H] N_2-Steam	26	1.84/6.08	0
[I] ODA-N_2-Steam	26	6.13/1.84/6.08	24.41
[J] N_2-ODA-Steam	26	1.84/6.13/6.08	22.56
[K] N_2-Steam-ODA	26	1.84/6.08/6.13	0

Notes: T_c denotes the temperature of the microfluidic pore network; P_f represents the pressure of injected fluid; The superscripts A-K denote different experimental cases; "-" denotes the injection sequence.

II was removed by purging with the designated injection fluid via the pump.

When the working fluids were injected, ports a and c on valve III were opened so that fluid could not flow through pore b of this valve. By opening the two-way valve of the corresponding branch, the working fluid (nitrogen or ODA) was injected via a high-pressure syringe pump (Table 1). A non-return valve (NRT) was used to prevent backflow. The back-pressure regulator (Valve I) was set to 6 MPa. The pressure in the tubing was monitored via a pressure sensor (PT). Once a steady flow was observed at the collector, ports a and c on valve II were opened so that the working fluid could be injected into the pore network at the preset pressure and flow rate.

For steam injection, deionized water in FR3 was first heated using a PID-controlled heating plate. Due to thermal losses between the heating unit and the pore network, the heating temperature was set slightly above the saturation temperature of steam at 6 MPa to ensure steam quality to be 1 at the inlet of pore network. A thermocouple was used to monitor the surface temperature of FR3. To reduce the heat loss along the flow path, heating ropes (McMaster-Carr, 3641K24) were wrapped around the tubing between FR3 and the three-way valve (Valve II), with a heating temperature of 303 °C. The back-pressure regulator (Valve I) was used to maintain the steam pressure in the tubing at 6 MPa. Once a steady steam flow was observed at the collector, ports a and c on valve II were opened so that steam could be injected into the pore network. The injection procedures for the dual fluids and ternary fluids were similar to those described above, with the only difference being the sequence of fluid injection.

(4) Soaking period

After fluid injection, ports b and c on valve II were opened, so as to seal the pore network for the simulation of the reservoir soaking process. The total time for injection and soaking was 30 min. After soaking, BPV-2 was depressurized to atmospheric pressure, and ports a and b on valve II were opened. Due to the pressure gradient, fluids (including heavy oil) within the pore network could flow toward the collector.

(5) Visual observation

During the injection, soaking and extraction stages, a high-speed camera was used to capture the evolution of oil phase distribution within the pore network at a frame rate of 60 fps. Each huff-and-puff experiment included four injection-soaking-extraction cycles.

(6) Post-experiment chip cleaning

After each experiment, the pore network and connecting tubes were cleaned by first injecting toluene at 50 μL/min to dissolve and flush out residual heavy oil, followed by DI water at 100 μL/min to remove any remaining toluene. Subsequently, the entire assembly, including the microfluidic pore network, metal fixture, capillary tubing, and valves, was placed in a vacuum oven and dried at 120 °C for 10 h to remove all solvent residues.

3. Result and discussion

A series of huff-n-puff experiments were conducted, and the corresponding conditions and results are summarized in Table 2. In some experiments, oil could be produced, whereas this was a mixture of heavy oil and the injected working fluids, which are difficult to be separated. Hence, the apparent recovery rate was introduced, which is defined as the ratio of the total mass of the produced mixture collected to the initial total mass of heavy oil contained in the microfluidic system:

$$\varphi = \frac{m_x}{m_o} \tag{6}$$

where m_x and m_o denote the mass of the produced mixture and the initial mass of heavy oil in the microfluidic system, respectively. $m_o = 4.27 \times 10^{-2}$ g.

It should be noted that the oil recovery efficiency cannot be calculated by tracking saturation changes within the pore network. This is because during the production process, an indeterminate amount of oil may flow into pore network from the tubing (between the network and valve III) which is initially oil filled. Consequently, the precise amount of oil produced through the port channel could not be determined. Therefore, the amount of oil mixture in the collector was used to evaluate the oil recovery performance.

The main objective of this study was to investigate the effects of injected fluids on heavy oil mobilization within the pore network. To this end, both the effects of individual fluids and their synergistic interactions were examined. For scenarios involving multiple injected fluids, the influence of injection sequence was also explored (e.g., experiments I to K in Table 2).

3.1 Huff-and-puff at different temperatures

In the steam huff-and-puff recovery of heavy oil, the primary function of steam is to heat oil and reduce its viscosity. In our experiments, however, the pore network was housed

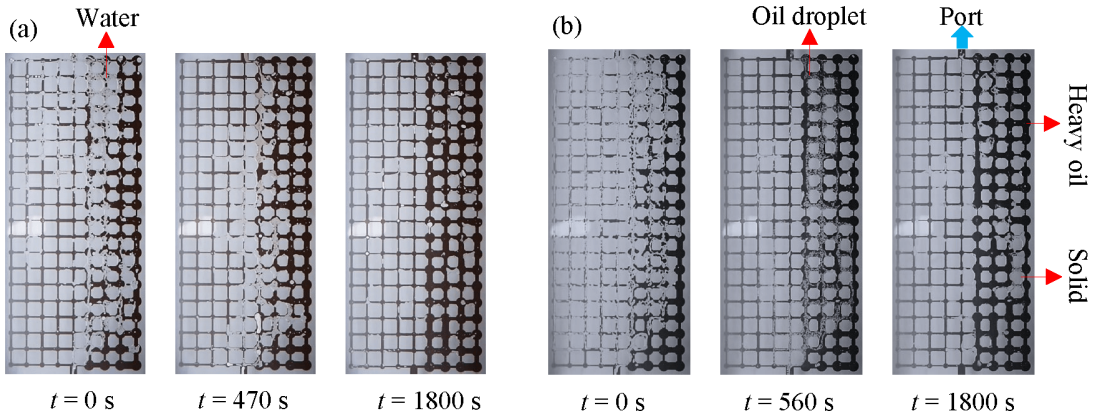

Fig. 3. Evolution of water and oil distribution during extraction in the first huff-and-puff cycle at (a) 50 °C and (b) 70 °C. Unless otherwise specified, $t = 0$ s and 1,800 s denote the initial and final stages, respectively, and the blue arrow indicates the port channel.

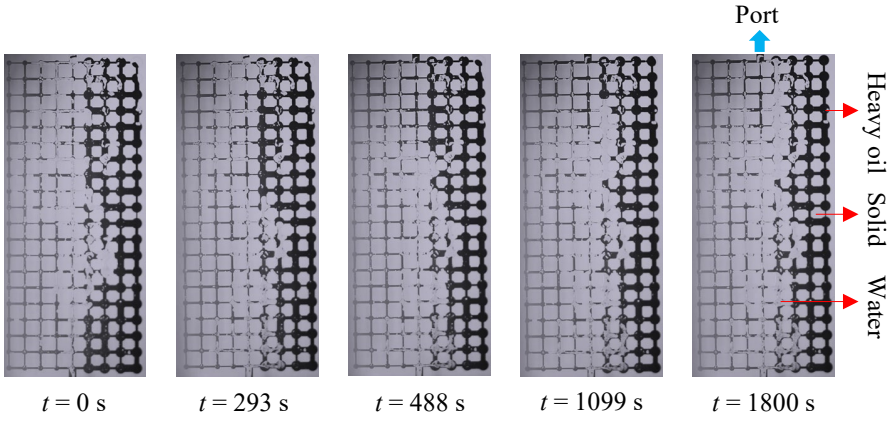

Fig. 4. Evolution of water and oil distribution in the pore network during extraction in the first huff-and-puff cycle.

in an aluminum fixture with high thermal capacity. Although saturated steam was injected at around 6 MPa, it condensed into water before entering the port channel of the pore network. The latent heat released during condensation was absorbed by the fixture, resulting in a limited temperature rise in the pore network. Measurements showed that the surface temperature of the pore network increased only slightly from 26.7 to 27.3 °C during steam injection (Fig. S8). Therefore, under the present experimental conditions, steam did not contribute significantly to heating the heavy oil. In addition, the replacement of the metallic fixture with alternative materials featuring improved thermal insulation, such as aerogels or polyether ether ketone, is not feasible due to their insufficient mechanical strength.

To investigate the effect of temperature on the mobilization of heavy oil inside the microfluidic pore network, independent temperature-controlled comparative experiments were also conducted (Experiments A and B in Table 2). The fixture was heated using a thermostatic stage (Fig. S9) to maintain pore-network temperatures of 50 and 70 °C. DI water was taken as the injection fluid. Oil was produced at the outlet of Passway II only at 70 °C, while no oil extraction was observed at 50 °C (Fig. 3(a)). The evolution of the water-oil distribution during oil extraction process at these temperatures is compared in Fig. 3.

As temperature increased from 50 to 70 °C, the oil viscosity decreased from approximately 1 to 0.5 Pa·s, which significantly influenced its mobilization. Notably, at 70 °C, numerous dispersed oil droplets were observed in the high-permeability region of the pore network during extraction (Fig. 3(b)), a phenomenon absent at 50 °C. These observations suggest that the elevated temperature not only reduced oil viscosity but might also lower the oil-water interfacial tension, thereby promoting the breakup of the continuous oil phase by DI water and enhancing pore-scale oil mobilization.

3.2 Huff-and-puff with individual injected fluid

To elucidate the individual roles of steam, N_2 and ODA in mobilizing heavy oil within the pore network, experiments C to E in Table 2 were conducted using each fluid separately.

3.2.1 Steam

As previously noted, when steam is injected, it condenses into liquid water before reaching the port channel of the pore network (Fig. S10). Following a 30 minute injection and soak period, the oil extraction process begins. Fig. 4 presents the evolution of the water oil distribution during extraction in the first huff and puff cycle. As pressure within the pore network declines, heavy oil in the high permeability zone moves along

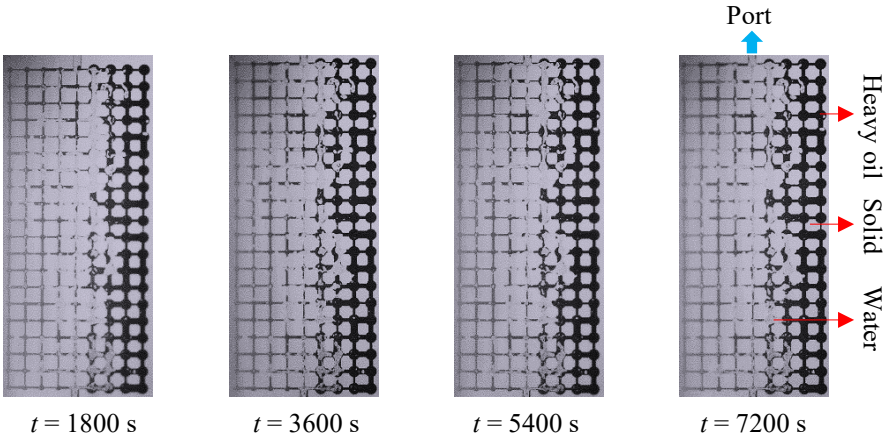

Fig. 5. Water and oil phase distribution at the end of extraction for the first (1,800 s), second (3,600 s), third (5,400 s), and forth (7,200 s) huff-and-puff cycle.

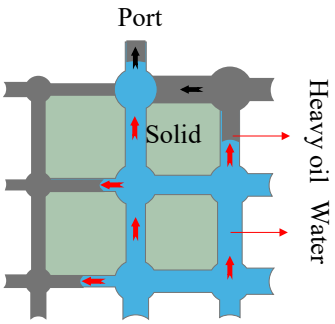

Fig. 6. Schematic of oil recovery when steam is the sole injected fluid (red arrows: Water migration path, black arrows: Heavy oil flow direction).

the interface between the low- and high-permeability regions. Concurrently, oil from the low-permeability region and areas near the port also migrates toward the port channel.

At the end of the first extraction cycle, a continuous water pathway connecting the injection port and outlet channel is established within the high-permeability zone. In subsequent huff-and-puff cycles, water predominantly follows this preferential flow path, resulting in minimal rearrangement of the remaining oil, as shown in Fig. 5. This result indicates that the early formation of such preferential flow channels can significantly limit the efficiency of oil recovery.

To further clarify the pore-scale displacement mechanism during steam huff-and-puff extraction, a schematic representation was constructed based on the experimental observations. Fig. 6 schematically illustrates the movement of heavy oil within the pore network during the extraction process. Condensed water displaces heavy oil in a piston-like manner within high-permeability regions. This process eventually forms a continuous water pathway connecting the inlet and outlet. Therefore, the subsequent water follows this path exclusively and stops displacing the remaining heavy oil.

3.2.2 N_2

Compared with carbon dioxide, the solubility of N_2 in heavy oil is significantly lower, with a molar fraction solubility of only about 0.009 at 2 MPa (Tong et al., 1999). Consequently, no bubble nucleation was observed during the pressure-depletion stage of N_2 huff-and-puff oil extraction, which clearly distinguishes its extraction mechanism from that of high-solubility gases such as CO_2. Based on the above results, N_2 is essentially immiscible with the heavy oil used in this study. When N_2 was used as the sole injected fluid, small gas bubbles adhering to the pore walls were observed after the N_2 injection (Fig. S11). Following a soaking period, oil extraction began. The evolution of the gas-oil distribution during this extraction stage is illustrated in Fig. 7. Obviously, as pressure in the pore network declined, the trapped gas bubbles expanded in the low- and high-permeability regions. This expansion not only displaced heavy oil but also broke up the continuity of the oil phase, thereby enhancing its overall mobility. It should be noted that the displacement behavior remained largely consistent across subsequent cycles for N_2 injection, because the residual heavy oil within the system was pushed back into the microfluidic chip during later fluid injections, allowing the heavy oil in the chip to maintain nearly the same initial saturation. Therefore, only the phase distribution during the first huff-and-puff cycle is discussed here.

To examine the movement of gas through the pore network in detail, Fig. 8 presents the evolution of the gas oil distribution within the regions highlighted by boxes in the right panel of Fig. 7. The region enclosed by the orange box is located closer to the port channel than that marked by the white box. As seen in Fig. 8(a), two bubbles (A and B) within the orange box region coalesce to form a larger bubble (C). Fig. 8(b) illustrates the pinch-off of a bubble (D) caused by the flow of heavy oil. The resulting fragmented bubbles become dispersed and trapped within the heavy oil, continuously perturbing the residual oil phase and enhancing its mobilization.

The variation in the area of bubbles A, B, C, and D (shown in Fig. 8) is presented in Fig. 9, where the normalized time is displayed. In the early stage, bubbles located at the chip wall typically exhibit regular circular geometries, which subsequently expand. Once their expansion becomes constra-

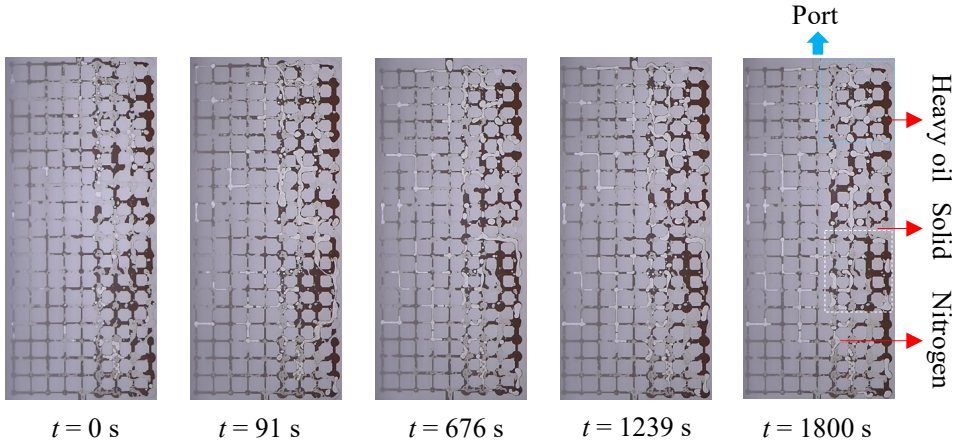

Fig. 7. Evolution of N_2 and oil distribution in the pore network during extraction in the huff-and-puff cycle.

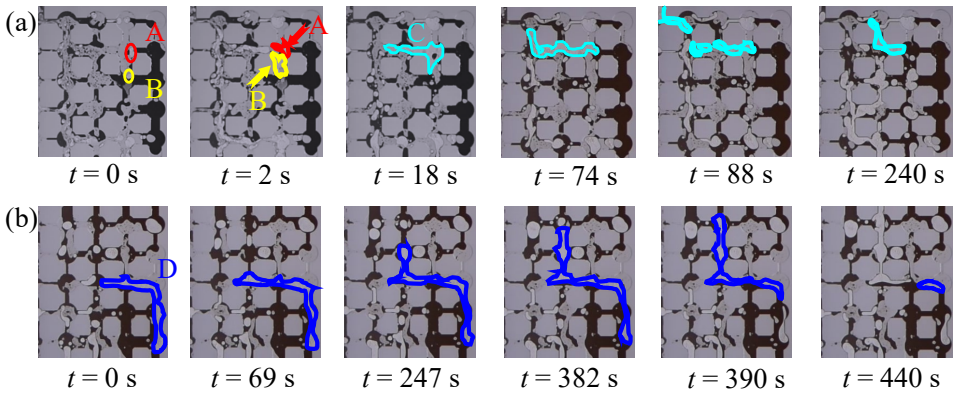

Fig. 8. Movement of gas bubbles in the regions marked by (a) an orange box and (b) a white box in the right panel of Fig. 7.

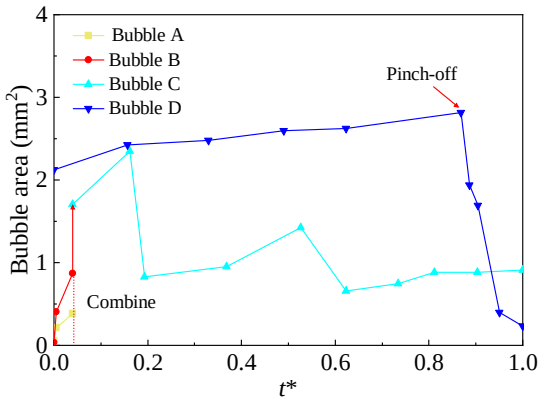

Fig. 9. Variation in bubble area with dimensionless time.

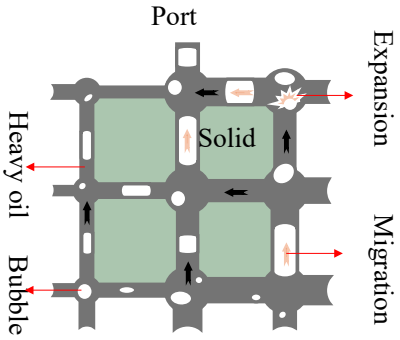

Fig. 10. Schematic of oil recovery when N_2 is the sole injected fluid (yellow arrows: N_2 bubbles migration path, and black arrows: Heavy oil flow direction).

ined by the pore walls, the bubble growth exhibits significant anisotropy, characterized by elongation toward the production port. When two neighboring bubbles A (0.39 mm^2) and B (0.87 mm^2) merge, they form a considerably larger bubble C (1.71 mm^2). Bubble C shows an irregular shape and spans several pore bodies and pore throats. This bubble exhibits pronounced periodic size fluctuations: Its area measures 2.35 mm^2 at $t^* = 0.16$, 0.84 mm^2 at $t^* = 0.19$, 0.95 mm^2 at $t^* = 0.37$, 1.43 mm^2 at $t^* = 0.53$, and 0.66 mm^2 at $t^* = 0.62$. Thereafter, the bubble area stabilizes. As for bubble D (Fig. 8b), its area increases to 2.81 mm^2 at $t^* = 0.87$, and it exhibits an irregular morphology due to geometric confinement by the pore structure and residual heavy oil. As Bubble D continues to grow toward the production port, it progressively coalesces with neighboring bubbles and extends along the connected pore throats. During this process, a narrow gas filament forms at the throat entrance as the bubble is strongly constrained by the pore geometry. With the subsequent pressure relaxation inside the bubble, the gas filament becomes unstable and eventually ruptures, leading to bubble pinch-off. After this event, the area of Bubble D is markedly reduced.

To clarify the pore-scale mechanisms governing heavy-oil

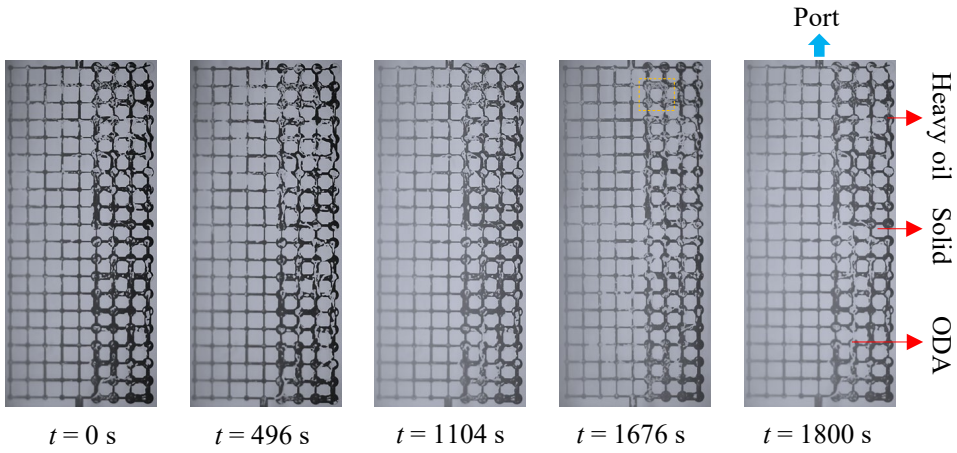

Fig. 11. Evolution of ODA and oil distribution in the pore network during extraction in the first huff-and-puff cycle.

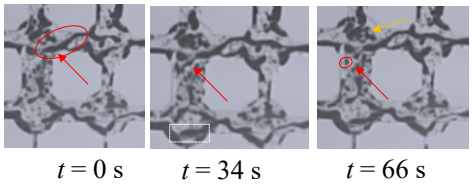

Fig. 12. Evolution of ODA and oil distribution within the region marked in Fig. 11.

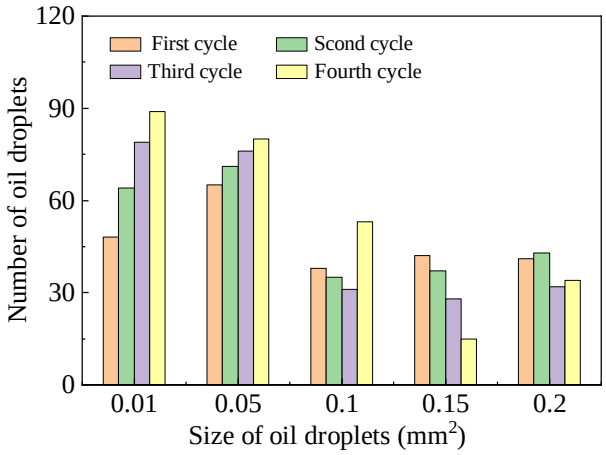

Fig. 13. Quantitative evaluation of ODA-induced heavy oil emulsification during multiple huff-and-puff cycles.

mobilization during N_2 huff-and-puff extraction, a schematic interpretation was developed based on the experimental observations. Fig. 10 schematically illustrates the movement of heavy oil within the pore network during N_2 huff-and-puff extraction. Gas expansion plays a decisive role in mobilizing the heavy oil. As the gas bubbles migrate toward the lower-pressure port channel, they drive a piston-like displacement of heavy oil in both the low- and high-permeability regions of the pore network.

3.2.3 ODA

To elucidate the influence of ODA on heavy oil movement during the huff-and-puff extraction process, the evolution of the ODA and oil phase distribution was analyzed. Fig. 11 shows the evolution of ODA and oil distribution during extraction when ODA was used as the sole injection fluid, while the evolution during the injection stage is presented in Fig. S12. As observed, numerous dispersed oil structures formed, particularly in high-permeability regions. These dispersed structures, generated through the interaction between ODA and heavy oil, enhanced the mobility of heavy oil.

To deeply examine the formation of dispersed oil structures, Fig. 12 presents the evolution of ODA and oil distribution within the region marked in Fig. 11. Driven by flow, the heavy oil is elongated into slender filaments, as indicated by the red arrows in Fig. 12. These filaments subsequently break up due to interfacial instability, leading to the generation of oil droplets. Emulsification between the ODA and oil phases, shown in light black and marked by the white box, is also observed. Furthermore, ODA is observed within the heavy oil, as indicated by the orange arrow in the right panel of Fig. 12.

The cumulative amount of the ODA injected over multiple injection cycles positively promotes heavy oil emulsification. To quantitatively assess the emulsification performance of ODA during repeated huff-and-puff operations, the evolution of heavy-oil morphology was analyzed by tracking the transformation of continuous oil into dispersed droplets. Fig. 13 presents a quantitative evaluation of the emulsification effect of ODA over four huff-and-puff cycles. The results show that when the droplet area is smaller than 0.1 mm^2, the number of small oil droplets in the pore network gradually increases with the number of huff-and-puff cycles. In contrast, for droplets larger than 0.1 mm^2, the droplet number continuously decreases as the cycle number increases. This trend indicates that the injection of ODA effectively promotes the dispersion of continuous heavy oil, and the emulsification effect becomes more pronounced with increasing cycle number. However, although a noticeable emulsification effect between ODA and heavy oil is observed, the actual injected mass of ODA is only 1.68×10^{-9} kg, which is far lower than the total mass of heavy oil within the pore network. Such a limited dosage significantly restricts the spatial coverage of ODA in the porous structure, resulting in most of the heavy oil not being effectively mobi-

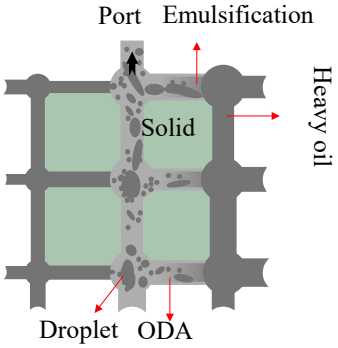

Fig. 14. Schematic of oil movement during the extraction process in the ODA huff-and-puff (black arrows: Flow direction).

lized and extracted.

To further interpret the pore-scale displacement mechanisms revealed by the experimental observations, a conceptual schematic was developed to summarize the migration behavior of heavy oil during ODA huff-and-puff extraction. Fig. 14 schematically illustrates the movement of heavy oil within the pore network. The primary role of ODA is to interact with the oil specifically within the high-permeability regions. In these zones, ODA permeates into the heavy oil, leading to emulsification and the formation of either dispersed oil droplets or elongated filamentary structures. To avoid potential misinterpretations, Fig. 14 is presented as a conceptual mechanism illustration synthesized from the discussed experimental observations and interfacial behavior, rather than as direct quantitative evidence. The schematic is intended to visually summarize the proposed emulsification pathway and phase evolution during the displacement process.

3.3 Huff-and-puff with dual injected fluids

In this section, the movement of heavy oil within the pore network during the extraction process of huff-and-puff with dual injected fluids (Experiments F-H in Table 2) is investigated. The dual injected fluids include N_2 followed by ODA injection sequence (N_2-ODA), ODA-Steam, and N_2-Steam. Oil extraction is observed at the outlet of passway 2 in the case of N_2-ODA, but not in the other two cases

3.3.1 N_2-ODA

Under this experimental case, effective heavy oil extraction was achieved. However, the actual mass of residual heavy oil remaining in the capillary channels after the first cycle could not be accurately determined, making it difficult to quantify the initial oil content in subsequent cycles and reliably evaluate the recovery performance during repeated extraction. Therefore, this study focuses on the first huff-and-puff cycle, in which the initial heavy-oil saturation is well defined. Fig. 15 illustrates the distribution evolution of ODA, N_2 and oil during the first extraction cycle, while the phase evolution during the injection stage is presented in Fig. S13. The image at $t = 0$ s corresponds to the end of the 30 minute soaking period. At this time, no N_2 bubbles are observed within the pore network; the injected N_2 is likely retained in the tubing connecting the pore network to Valve II (see Fig. 2). However, there is visible emulsion in the $t = 0$ s image. Due to its higher mobility compared to heavy oil, this emulsion is extracted first, as seen in the image at $t = 43$ s. Subsequently, N_2 from the tubing connecting the pore network to Valve II enters the pore network. Notably, clusters of microbubbles emerge (see image at $t = 62$ s). Heavy oil is retained between these microbubbles, forming an oil-in-microbubble cluster structure. These clusters exhibit higher mobility than heavy oil alone, primarily due to the significantly lower viscosity of the gas. As a result, the oil-in-microbubble clusters migrate toward the port channel. After this, ODA from the tubing connecting the pore network to Valve II flows into the pore network, which may be due to bubble expansion in the tubing. This in turn leads to formation of emulsion, enabling the further recovery of heavy oil ($t = 731$ s). At the end stage of extraction, some discrete bubbles are observed in heavy oil ($t = 1{,}800$ s). The bubble expansion, however, is not observed.

Certain differences in gas behavior during extraction should be noted between the experiments using pure N_2 and those using N_2-ODA. In the pure N_2 experiments, bubbles are observed at the start of extraction, and their expansion within the pore network is also visible. In contrast, in the N_2-ODA experiments, no bubbles are seen in the pore network at the beginning of extraction. Instead, the injected gas remains in the tubing connecting the pore network to valve II. Gas expansion is considered to also occur within this tubing, even though it cannot be directly observed. This expansion drives ODA in the tubing into the pore network and consequently extraction of oil. Once the gas enters the pore network, oil-in-microbubble clusters form, which is primarily due to the influence of ODA. These microbubble clusters, which are beneficial for oil extraction, were not observed in experiments using only N_2. The pore structure constraints also drive the formation of these microbubble clusters. Fig. 16 records the dynamic evolution of a continuous gas bubble flow into microbubbles. When these bubbles pass through a pore throat, the imbalance between the capillary pressure at the throat and the internal bubble pressure causes bubble pinch-off. During this process, the leading bubble continuously migrates forward, while the trailing, unexpanded bubble is strongly sheared by the high-velocity heavy oil phase. When the shear force exceeds the interfacial tension, the bubble undergoes further breakup. Ultimately, the combined effects of repeated pinch-off and shear fragment the trailing bubble into a large number of microbubbles.

To synthesize the experimental observations and clarify the underlying recovery mechanisms in the N_2-ODA huff-and-puff process, a conceptual model is proposed. Fig. 17 illustrates the proposed oil-recovery mechanism: Fig. 17(a) Emulsion formation through the interaction of ODA with heavy oil; Fig. 17(b) formation of oil-in-microbubble clusters driven by the combined effects of ODA, gas and heavy oil. Gas expansion within the tubing connecting the pore network and valve II, although not observed (thus not shown in Fig. 17), also benefit the mobility of heavy oil.

3.3.2 ODA-Steam and N_2-Steam

For the huff-and-puff experiments involving ODA-Steam and N_2-Steam (corresponding to experiments G and H in

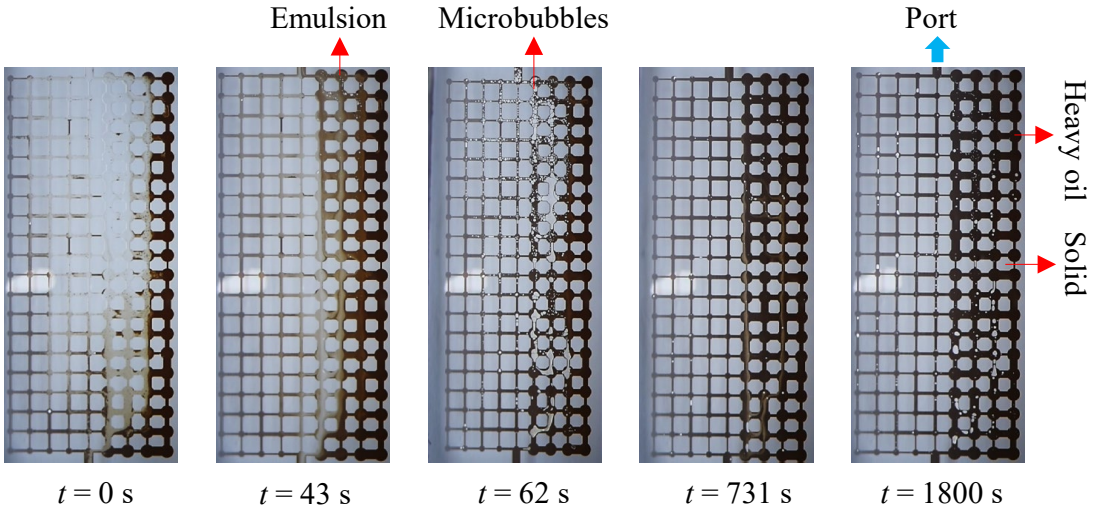

Fig. 15. Evolution of ODA, N_2 and oil phases during the extraction of first cycle of the ODA-N_2 huff-and-puff.

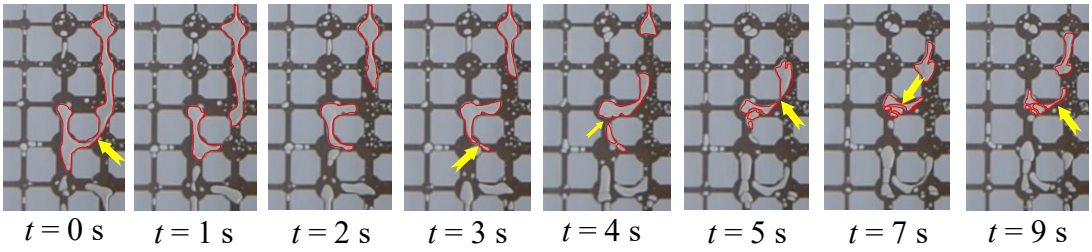

Fig. 16. Evolution of continuous gas bubble flow forming microbubbles driven by pore structure constraints (yellow arrows: Location of bubble break, red irregular solid line: Gas bubble).

Table 2), no oil extraction was observed at the outlet of passway II. As noted earlier, steam condenses into liquid water before entering the pore network. In the ODA-Steam case, the condensed water dilutes the ODA, reducing its ability to form an emulsion. Furthermore, the absence of bubble expansion under these conditions also contributes to the lack of oil extraction (Fig. S14). The N_2-Steam case behaves similarly to the pure N_2 scenario, where no oil is produced, largely due to the high viscosity of the heavy oil (Fig. S15).

3.4 Huff-and-puff with ternary injected fluids

In the huff-and-puff experiments involving ternary injected fluids, the effects of different injection sequences were investigated. Three configurations were examined: ODA-N_2-Steam, N_2-ODA-Steam, and N_2-Steam-ODA. As shown in Table 2, oil extraction can be observed at the outlet of passway II in the first two cases, but not in the third case. Although the injection order of ODA and N_2 differs between the first and second cases, our experiments show that N_2 enters the pore network first during injection in both configurations. This behavior is primarily attributed to the significantly lower viscosity and higher mobility of N_2 compared to ODA. In addition, the large compressibility of N_2 allows it to respond more rapidly to pressure gradients in the microfluidic system, while capillary entry pressure further favors the preferential invasion of the low-viscosity gas phase into the pore network. These combined effects lead to the earlier appearance of N_2 in the microfluidic chip, even when it is injected after ODA. Therefore, these two cases can effectively be regarded as following the N_2-ODA-Steam sequence.

Since steam condenses into liquid water before entering the pore network, the N_2-ODA-Steam extraction process (shown in Fig. S16) essentially resembles that of N_2-ODA. The key difference lies in the reduced ODA concentration in the ternary fluid case, which weakens the interactions between ODA, gas bubbles and heavy oil. For example, as shown in Fig. 18, the number of microbubbles with a size ≤ 0.05 mm^2 is significantly lower in the ternary fluid system compared to the dual-fluid case.

In the N_2-Steam-ODA sequence, water enters the pore network before ODA during injection. As a result, the effective concentration of ODA reaching the pore network is significantly lower compared to the N_2-ODA-Steam case. This reduction in ODA concentration leads to lower emulsion formation, which is likely the primary reason why no oil extraction is observed in the N_2-Steam-ODA configuration (Fig. S17).

4. Conclusions

In this work, microfluidic pore network experiments were conducted to investigate the flow behavior of heavy oil within reservoir pores during N_2 and ODA-assisted steam huff-and-

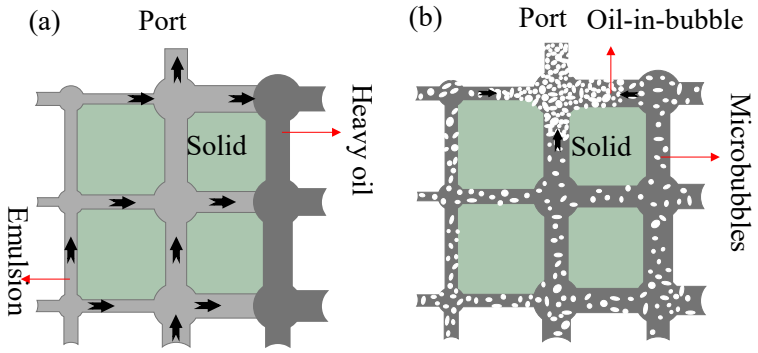

Fig. 17. Schematic of oil movement during the extraction process in N_2-ODA huff-and-puff: Formation of (a) emulsion and (b) oil-in-microbubble clusters (black arrows: Flow direction, yellow arrow: Migration path of N_2 bubbles).

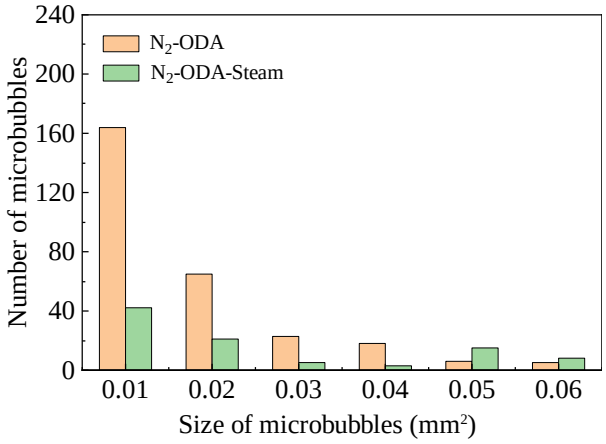

Fig. 18. Size distribution of microbubbles under the ternary injection (N_2-ODA-steam) and dual injection (N_2-ODA) schemes.

puff processes, and the roles of the injected fluids were systematically examined. Although effective heat transfer from steam to oil is limited by the high specific heat capacity of the fixture, additional independent temperature-controlled experiments confirmed that steam injection reduces heavy-oil viscosity and enhances its mobility. Injected gas bubbles expand to displace heavy oil, and ODA promotes the formation of emulsion and oil-in-microbubble clusters, both of which exhibit higher mobility than bulk heavy oil. On the other hand, steam condensation can dilute ODA, weakening its interaction with heavy oil and gas bubbles and thus inhibiting the formation of emulsion and microbubble clusters. Furthermore, the injection sequence was shown to significantly influence heavy oil recovery. These results provide valuable insights for optimizing heavy oil recovery strategies.

Acknowledgements

The authors are grateful for the support of Research Project of Sinopec Corp.: “Study on Thermal Composite Development Technology for Multilateral Horizontal Wells in Shengli Heavy Oil Fields” (No. P25035).

Supplementary file

https://doi.org/10.46690/capi.2026.04.01

Conflicts of interest

The authors declare no competing interest.

References

Ahmadi, M., Chen, Z. Challenges and future of chemical assisted heavy oil recovery processes. Advances in Colloid and Interface Science, 2020, 275: 102081.

Arabloo, M., Ghazanfari, M. H., Rashtchian, D. Microfluidic study of surfactant flooding of heavy oil in layered porous media containing fractures. The Canadian Journal of Chemical Engineering, 2024, 102(5): 1970-1991.

Bai, J., Gu, T., Tao, L., et al. The enhanced oil recovery mechanisms in heavy oil reservoirs by chemical compound flooding after multiple cycles of huff-n-puff. Energy & Fuels, 2025, 39(13): 6220-6231.

Bao, B., Riordon, J., Mostowfi, F., et al. Microfluidic and nanofluidic phase behaviour characterization for industrial CO_2, oil and gas. Lab on a Chip, 2017, 17(16): 2740-2759.

De Haas, T. W., Fadaei, H., Guerrero, U., et al. Steam-on-a-chip for oil recovery: The role of alkaline additives in steam assisted gravity drainage. Lab on a Chip, 2013, 13: 3832-3839.

Fan, J., He, Z., Pang, W., et al. Experimental study on the mechanism and development effect of multi-gas assisted steam huff and puff process in the offshore heavy oil reservoirs. Journal of Petroleum Exploration and Production Technology, 2021, 11: 4163-4174.

Gao, C., Shi, J., Zhao, F. Successful polymer flooding and surfactant-polymer flooding projects at Shengli Oilfield from 1992 to 2012. Journal of Petroleum Exploration and Production Technology, 2014, 4: 1-8.

Gizzatov, A., Pierobon, S., AlYousef, Z., et al. High-temperature high-pressure microfluidic system for rapid screening of supercritical CO_2 foaming agents. Scientific Reports, 2021, 11(1): 3360.

Gomaa, S., Salem, K. G., El-Hoshoudy, A. N. Enhanced heavy and extra heavy oil recovery: Current status and new

trends. Petroleum, 2024, 10(3): 399-410.

Gong, H., Qin, X., Shang, S., et al. Enhanced shale oil recovery by the huff and puff method using CO_2 and cosolvent mixed fluids. Energy & Fuels, 2020, 34(2): 1438-1446.

Guo, Y., Liu, F., Qiu, J., et al. Microscopic transport and phase behaviors of CO_2 injection in heterogeneous formations using microfluidics. Energy, 2022, 256: 124524.

Hao, H., Hou, J., Zhao, F., et al. N_2-foam-assisted CO_2 huff-n-puff process for enhanced oil recovery in a heterogeneous edge-water reservoir: Experiments and pilot tests. RSC Advances, 2021, 11(2): 1134-1146.

He, H., Li, Q., Zheng, H., et al. Simulation and evaluation on enhanced oil recovery for steam huff and puff during the later phase in heavy oil reservoir – A case study of block G in Liaohe oilfield, China. Journal of Petroleum Science and Engineering, 2022, 219: 111092.

He, Q., He, B., Li, F., et al. Fractal characterization of complex hydraulic fractures in oil shale via topology. Energies, 2021, 14(4): 1123.

Heijkoop, S., Rieder, D., Moura, M., et al. A statistical analysis of fluid interface fluctuations: Exploring the role of viscosity ratio. Entropy, 2024, 26(9): 774.

Hu, H., Wu, S., Zhang, Y., et al. State-of-the-art of heavy-oil development in China and its technology challenges. Paper SPE 10617 Presented at SPE International Thermal Operations and Heavy Oil Symposium, Calgary, Alberta, Canada, 1-3 November 2005.

Huang, F., Xu, R., Jiang, P., et al. Pore-scale investigation of CO_2/oil exsolution in CO_2 huff-n-puff for enhanced oil recovery. Physics of Fluids, 2020, 32(9): 092011.

Lei, Z., Liu, Y., Wang, R., et al. A microfluidic experiment on CO_2 injection for enhanced oil recovery in a shale oil reservoir with high temperature and pressure. Energies, 2022, 15(24): 9461.

Li, L., Zheng, J., Shi, Y., et al. Mechanisms of fluid migration and CO_2 storage in low permeability heavy oil reservoirs using high-pressure microfluidic CO_2 flooding experiment. Energy & Fuels, 2024, 38(9): 7997-8008.

Li, S., Lu, C., Wu, M., et al. New insight into CO_2 huff-n-puff process for extraheavy oil recovery via viscosity reducer agents: An experimental study. Journal of CO_2 Utilization, 2020, 42: 101312.

Lu, H., Huang, F., Jiang, P., et al. Exsolution effects in CO_2 huff-n-puff enhanced oil recovery: Water-oil-CO_2 three-phase flow visualization and measurements by micro-PIV in micromodel. International Journal of Greenhouse Gas Control, 2021, 111: 103445.

Mahardika, M., She, Y., Shori, F., et al. Enhanced heavy oil recovery by calcium hydroxide flooding with the production of viscoelastic materials: Study with 3-D X-ray tomography and 2-D glass micromodels. Energy & Fuels, 2021, 35(14): 11210-11222.

McBride, S. A., Temprano-Coleto, F., Kaneelil, P. R., et al. Effect of capillary number and viscosity ratio on multiphase displacement in microscale pores. Physical Review Fluids, 2025, 10(5): 054201.

Nguyen, P., Carey, J. W., Viswanathan, H. S., et al. Effectiveness of supercritical-CO_2 and N_2 huff-and-puff methods of enhanced oil recovery in shale fracture networks using microfluidic experiments. Applied Energy, 2018, 230: 160-174.

Owolabi, A. O., Dyam, P. L. Pressure distribution in a layered reservoir with gas-cap and bottom water. Nigerian Journal of Technology, 2012, 31: 189-198.

Pratama, R. A., Babadagli, T. A review of the mechanics of heavy-oil recovery by steam injection with chemical additives. Journal of Petroleum Science and Engineering, 2022, 208: 109717.

Rayleigh. The principle of similitude. Nature, 1915, 95(2368): 66-68.

Saadat, M., Vikse, N. B., Øye, G., et al. A microfluidic study of oil displacement in porous media at elevated temperature and pressure. Scientific Reports, 2021, 11(1): 20349.

Schumi, B., Clemens, T., Wegner, J., et al. Alkali/cosolvent/polymer flooding of high-TAN oil: Using phase experiments, micromodels, and corefloods for injection-agent selection. SPE Reservoir Evaluation & Engineering, 2020, 23(2): 463-478.

Su, H., Zhou, F., Zheng, A., et al. Heavy oil recovery by alkaline-cosolvent-polymer flood: A multiscale research using micromodels and computed tomography imaging. SPE Journal, 2022, 27(3): 1480-1492.

Sun, H., Wang, H., Cao, X., et al. Innovations and applications of the thermal recovery techniques for heavy oil. Energy Geoscience, 2024, 5(4): 100332.

Tao, L., Chen, Y., Liu, N., et al. A novel experimental method for the evaluation of residual oil distribution in a sand-packed model by using nitrogen and viscosity reducer huff-puff technology to develop heavy oil reservoirs. Journal of Petroleum Science and Engineering, 2022, 208: 109585.

Tong, J., Gao, W., Robinson, R. L., et al. Solubilities of nitrogen in heavy normal paraffins from 323 to 423 K at pressures to 18.0 MPa. Journal of Chemical & Engineering Data, 1999, 44(4): 784-787.

Vavra, E., Puerto, M., Biswal, S. L., et al. A systematic approach to alkaline-surfactant-foam flooding of heavy oil: Microfluidic assessment with a novel phase-behavior viscosity map. Scientific Reports, 2020, 10(1): 12930.

Wan, T., Wang, X., Jing, Z., et al. Gas injection assisted steam huff-n-puff process for oil recovery from deep heavy oil reservoirs with low-permeability. Journal of Petroleum Science and Engineering, 2020, 185: 106613.

Wang, H., Wei, B., Hou, J., et al. Heavy oil recovery in blind-ends during chemical flooding: Pore scale study using microfluidic experiments. Journal of Molecular Liquids, 2022, 368: 120724.

Wang, Z., Du, H., Li, S., et al. Experimental study on gas-assisted cyclic steam stimulation under heavy-oil sandstone reservoir conditions: Effect of N_2/CO_2 ratio and foaming agent. Geoenergy Science and Engineering, 2023, 228: 211976.

Wei, J., Zhou, X., Zhou, J., et al. CO_2 huff-n-puff after surfactant-assisted imbibition to enhance oil recovery for

tight oil reservoirs. Energy & Fuels, 2020, 34(6): 7058-7066.

Xiong, R., Guo, J., Kiyingi, W., et al. Technical transformation of heavy/ultra-heavy oil production in China driven by low carbon goals: A review. Journal of Cleaner Production, 2024, 458(4): 142531.

Xiong, X., Sheng, J. J., Wu, X., et al. Experimental investigation of foam-assisted N_2 huff-n-puff enhanced oil recovery in fractured shale cores. Fuel, 2022, 311: 122597.

Xu, L., Abedini, A., Qi, Z., et al. Pore-scale analysis of steam-solvent coinjection: Azeotropic temperature, dilution and asphaltene deposition. Fuel, 2018, 220: 151-158.

Yu, W., Zhou, X., Kanj, M. Y. Microfluidic investigation of foam coarsening dynamics in porous media at high-pressure and high-temperature conditions. Langmuir, 2022, 38(9): 2895-2905.

Zhang, G., Mo, C., Tang, Y., et al. Impact of high-cycle huff and puff on residual oil distribution in heavy oil reservoirs. Geoenergy Science and Engineering, 2026, 256: 214168.

Zou, B., Pu, W., Zhou, X., et al. Experimental study on the feasibility of nitrogen huff-n-puff in a heavy oil reservoir. Chemical Engineering Research and Design, 2022, 184: 513-523.